An Anisotropic Etching Effect in the Graphene Basal Plane

By *Rong Yang, Lianchang Zhang, Yi Wang, Zhiwen Shi, Dongxia Shi, Hongjun Gao, Enge Wang*, and *Guangyu Zhang**

Graphene shows great potential for future electronics due to its extraordinary electrical properties and structure-engineerable nature.[1–3] Control of the edge structure of graphene is crucial during the fabrication process because the electrical, magnetic, and electrochemical properties of graphene are dependent on it, especially in quantum-confined graphene structures.[4–18] Electron-beam lithography and isotropic plasma etching are usually used for patterning graphene nanostructures. However, it is difficult to identify the crystallographic orientation and achieve smooth graphene edges simultaneously during fabrication, and one must therefore contend with graphene nanostructures with unknown crystallographic orientation and irregular edges.[4,5] Anisotropic etching has been proposed as a key technique for controllable graphene edge fabrication with atomic precision. So far, anisotropic etching of graphene has been realized by either catalytic nanoparticle cutting[19–22] or selective reaction of oxidized graphene with a SiO_2 substrate,[23] but it is difficult to apply such methods to a practical fabrication process because they are either substrate-limited or the cutting position, direction, and speed are not controllable. In this paper, we report a dry, anisotropic etching method for graphite and graphene. We are able to control the etching from the edges by tuning etching parameters such as plasma intensity, temperature, and duration. The etching process is attributed to hydrogenation and volatilization of carbon atoms and the etching dynamics are consistent with methane formation. This simple, clean, controllable, and scalable technique is compatible with existing semiconductor processing technology.

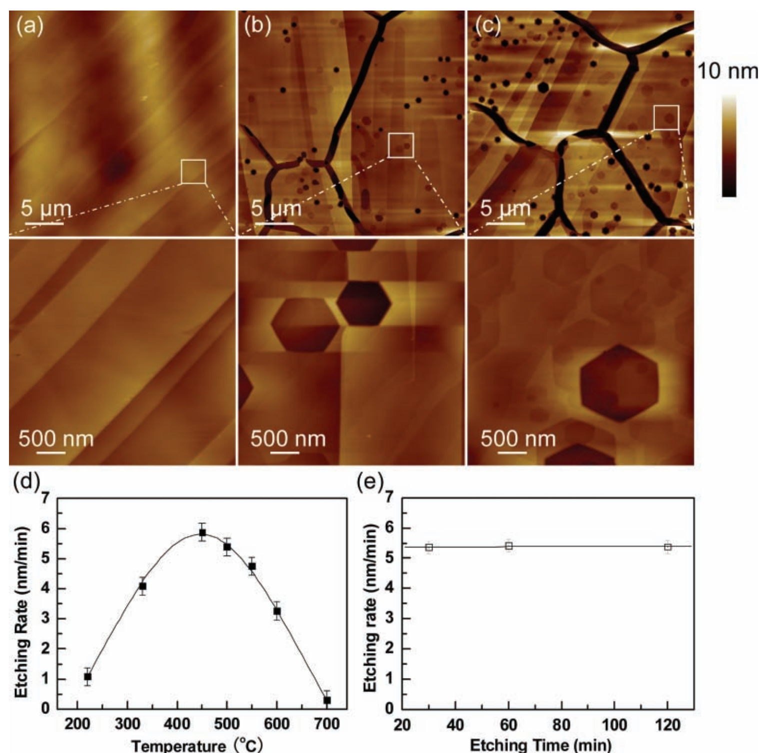

Figure 1. Anisotropic etching of graphite by H_2-plasma. a–c) AFM images of pristine, 50 W plasma-etched, and 100 W plasma-etched graphite. Plasma etching was performed at 500 °C for 2 h. Magnified images for the marked areas are shown. d) Measured maximum etching rate of graphite at various etching temperatures. The plasma power was 100 W. Solid lines represent Lorentzian line shape fits. e) Average etching speeds for graphite at different etching time intervals. The etching temperature was 500 °C.

Anisotropic etching was first applied to graphite because it consists of stacked graphene layers. The graphite samples with freshly cleaved surfaces were exposed to a pure hydrogen plasma for etching (see Supporting Information). An atomic force microscopy (AFM) image of a fresh graphite surface (**Figure 1a**) showed many stepped edges. Figures 1b and 1c show two typical AFM images of the graphite surface after etching with plasma powers of 50 and 100 W, respectively. The topographical features of the graphite surface are remarkably different after etching – trenches form at grain boundaries, and, more importantly, hexagonal pits form in the graphite basal plane. These regular hexagonal pits, which have the same orientations across the entire crystal grain, are clear indicators of anisotropic etching of the graphite basal plane, as graphite crystals possess sixfold rotational symmetry about [0001]. The formation of trenches and pits indicates that the etching initiates at the step edges as well as at the defect sites, which are more reactive due to the existence of dangling bonds or lattice

[*] R. Yang, L. Zhang, Prof D. Shi, Prof. H. Gao, Prof. G. Zhang
Nanoscale Physics and Device Lab
Institute of Physics
Chinese Academy of Science
Beijing 100190 (P.R. China)
E-mail: gyzhang@aphy.iphy.ac.cn
Dr. Y. Wang, Z. Shi, Prof. E. Wang
Surface Physics Lab
Institute of Physics, Chinese Academy of Science
Beijing 100190 (P.R. China)

DOI: 10.1002/adma.201000618

© 2010 WILEY-VCH Verlag GmbH & Co. KGaA, Weinheim
WILEY InterScience DISCOVER SOMETHING GREAT

distortion. We note that the etching is also highly anisotropic along the graphite *c*-axis.

Radiofrequency (RF) power is a key parameter for etching, and stronger plasma etching produces wider trenches and larger pits (see Figure 1b and c). Stronger or longer-time plasma etching also produces more defects in the graphite basal plane, extrapolated from the fact that more numerous etched pits were formed in these cases (see Figure S1, Supporting Information). Etching temperature is another key parameter, which was varied from 200 to 700 °C (see Figure S2 in the Supporting Information for more images). Interestingly, the etching speed is temperature dependent (Figure 1d); it increases with temperature, peaks at ≈450 °C, and then diminishes to zero at ≈700 °C. The "etching speed" here refers to the maximum etching speed in the graphite basal plane, estimated from the largest etched hexagonal pits. The average etching speeds in the graphite basal plane at different time intervals are plotted in Figure 1e. They reveal a constant etching speed, independent of time, under the same etching conditions (also see Figure S1 in the Supporting Information for more images).

Anisotropic etching effects for graphene by H_2-plasma etching are essentially the same as for graphite, independent of the etching speed. Typical AFM images of monolayer, bilayer, and multilayer graphene on SiO_2 substrates after etching are shown in **Figure 2a**, b, and c, and similar temperature-dependent, anisotropic etching speeds for monolayer and bilayer graphene are shown in Figure 2d. Note that the etching speed of monolayer graphene is higher than that of bilayer graphene or graphite under the same etching conditions. This higher etching speed for monolayer graphene may result from both the larger cross-sectional area for the reaction when exposing graphene edges to the plasma and the substrate-induced roughness. The low-power plasma anisotropic etching is used to etch only along edges and inherent defects, which does not induce other defects, and allows tailoring of graphene with precise control.

Considering that hydrogen radicals are the major reactive species in a H_2-plasma, we describe the etching process as hydrogenation and volatilization of reactive carbon sites by these radicals. In the graphite or graphene basal plane, H-radicals attack the carbon atoms at both edges and at surface defects via C-H covalent bond formation (hydrogenation) and C-C bond breakage (volatilization), and methane is the main product of the reaction. The maximum etching speed temperature of ≈450 °C is determined by the thermodynamic instability

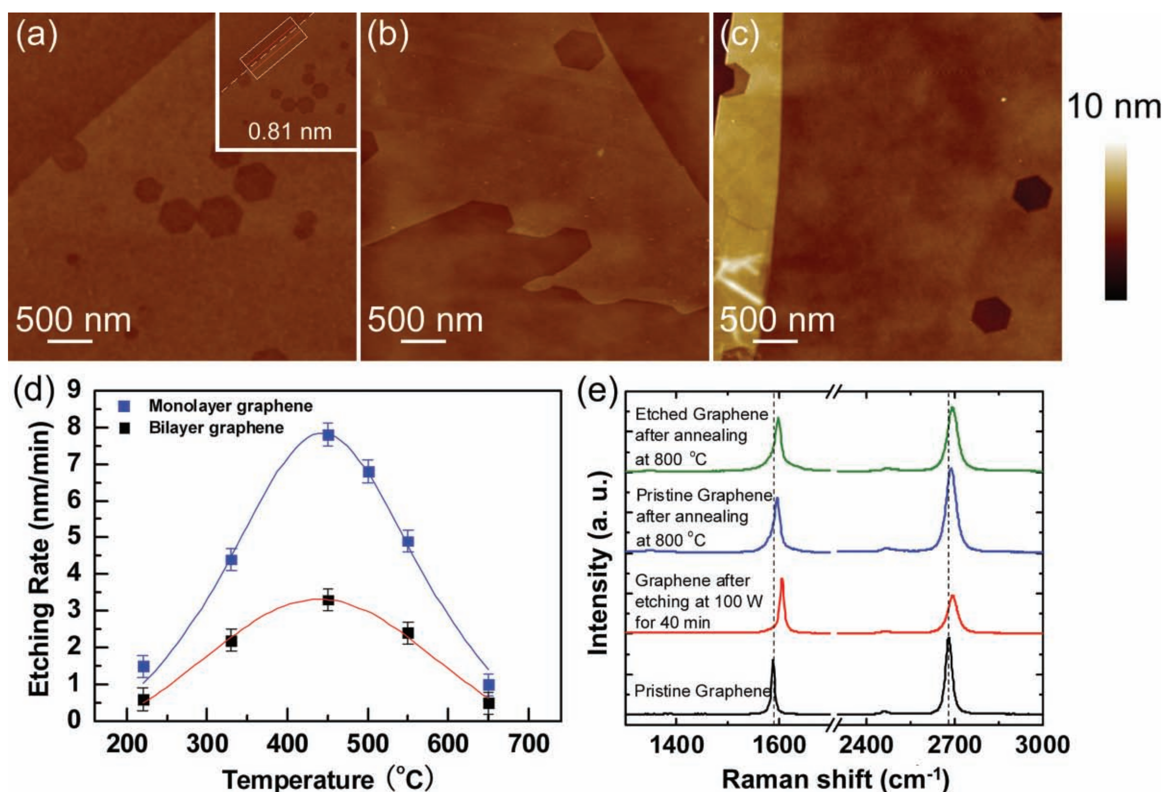

Figure 2. Anisotropic etching of graphene by H_2-plasma. a–c) AFM images of monolayer, bilayer, and multilayer graphene after H_2-plasma etching at 50 W and 500 °C for 20, 40 and 60 min, respectively. d) Measured maximum etching speed for both monolayer graphene (blue) and bilayer graphene (black) at various etching temperatures. The plasma power was 50 W. e) Raman spectra of pristine graphene (black), annealed graphene (blue), etched graphene (red), and etched graphene after annealing (green). The etching was performed at 500 °C for 40 min using a 50 W plasma and the annealing was performed at 800 °C for 1 h in vacuum. The fingerprint peaks, D, G, and 2D, are marked in the figure with peak positions at around 1340, 1590, and 2680 cm^{-1}, respectively.

© 2010 WILEY-VCH Verlag GmbH & Co. KGaA, Weinheim

of methane at this temperature.[24] C-C bond breaking depends directly on local bonding configurations and this is the origin of etching anisotropy. A hexagonal pit with zigzag edges will grow when a reaction starts from a surface vacancy. An atom-by-atom removal process is shown in the Supporting Information.

In order to identify the etching anisotropy in the graphite basal plane, we imaged the edges of the etched hexagonal pits using scanning tunneling microscopy (STM). We focused on the monolayer pits because their step edges can be clearly seen. **Figure 3a** shows a typical constant-current STM image of a hexagonal pit. The atomic resolution image of an edge is shown in Figure 3b. The good lattice structure of both the etched-top monolayer and the exposed underlying layer are clearly seen. Excluding the effects of drift distortion, we find that the angle of the graphite lattice is approximately normal to the edge, and therefore we assign the edge structure to the zigzag edge. Near the edges, we observed superstructure with a periodicity larger than that of graphite lattice (Figure 3b). The superstructure appears to be $(\sqrt{3}*\sqrt{3})$ $R30°$, as indicated by the inner set of spots in the two-dimensional Fourier transform spectrum shown in Figure 3c. These standing waves in the local density of states,[25] persisting to about 3 nm into the bulk layer, originate from the interference of coherently scattered surface-state electrons from the zigzag edges. We imaged many etched pits and found that their edges are always along the zigzag direction with an edge roughness of <2 nm with a window size of 100 nm. These observations reveal that the zigzag edge is the most stable edge structure under H_2-plasma etching, consistent with previous results from edge reconstruction via thermal annealing.[26–28] As illustrated in Figure 3d, the maximum etching speed along $[2\bar{1}\bar{1}0]$ and the minimum etching speeds along $[10\bar{1}0]$ can thus be deduced with a ratio of $2/\sqrt{3}$. Note that all the etching speed data in our experiment were measured along $[2\bar{1}\bar{1}0]$. Current/Voltage (I/V) characteristics were measured at 77 K between the STM tip and the etched graphite at different sites (see Figure S3, Supporting Information). The conductance at the edge is clearly lower than at the graphite basal plane due to the localization of electrons at the edges being passivated by hydrogen.[29–34]

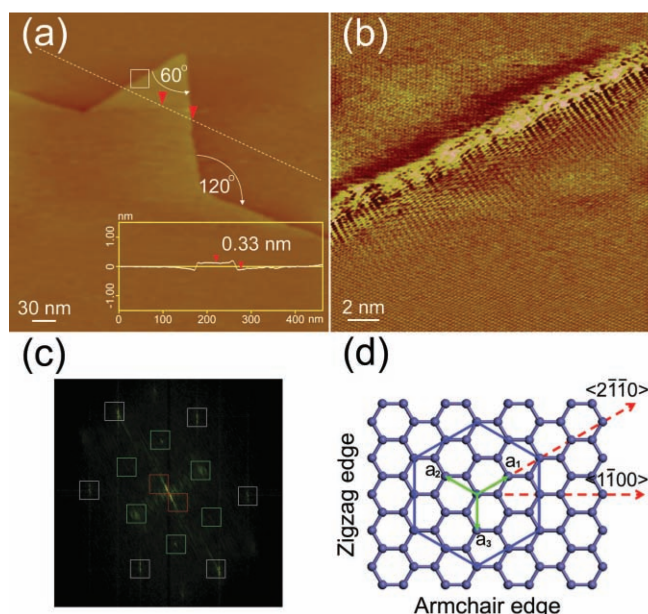

Figure 3. STM characteristics for etched hexagonal pits on graphite. a) STM image of a monolayer of hexagonal pits with the height profile shown in the inset. Images were scanned in air at room temperature with a Pt/Ir tip at a constant current of 1 nA and a bias of 50 mV. The cross-sectional cut of the STM topography is presented in order to illustrate the monolayer pit depth. b) Atomic resolution image for the region marked in a), with the step edge clearly visible. The image distortion was caused by thermal drift during scanning. c) The Fourier transform (FT) spectrum (power spectrum) of image (b). The Fourier components associated with the graphite lattice and the superstructure lattice are marked with white and green, respectively. d) Schematic drawing of a hexagonal graphene lattice. a1, a2, and a3 denote the axes in the basal plane. The blue hexagon is drawn to depict an etched pit. Zigzag and armchair edges are illustrated.

The quality of graphene after etching is a major concern when it is intended for use in electronic applications. STM data already show that graphite surfaces retain a perfect lattice structure after etching. To further demonstrate the quality of the etched graphene, we characterized it using Raman spectroscopy because the Raman D (disordered) mode is very sensitive to defects.[35] Figure 2e shows typical Raman spectra of two graphene samples on SiO_2. One sample was pristine and the other was etched. Raman spectra of both samples after high-temperature annealing are also included for better comparison. After etching, the Raman spectra show several changes including the appearance of a negligible D peak, a drastic decrease in the 2D (D overtone) peak intensity, and a blue-shift of both the G (graphitic mode) and 2D peaks. However, Raman features for both samples after annealing are nearly the same in terms of peak position, full width at half-maximum (FWHM), and relative intensity, which indicates that quality is still the same after etching (see Supporting Information, Table S1, for further discussion). We have also studied the electrical properties of natural graphene on SiO_2/Si before and after etching and obtained similar results (see Supporting Information).

Theoretical calculations predict that the graphene electronic structure depends strongly on its edges.[10–18] However, experimental proof[9,10,36–40] is lacking due to the difficulties associated with achieving well-defined edges. A very important application of anisotropic etching is the fabrication of graphene patterns with well-defined edges along designated crystallographic directions. In order to identify the crystallographic orientation of a graphene sample, plasma pre-etching for a short time is necessary to etch a few indicative hexagonal pits. To minimize the defects induced by etching, the pre-etching can be limited to a small part of the sample by masking the rest. A pilot study of making graphene nanoribbons (GNRs) with zigzag edges was carried out using the procedures illustrated in **Figure 4a** (see also Figure S5 in the Supporting Information). Mechanically cleaved graphene was first put onto SiO_2 substrates with alignment marks. The samples were then etched briefly to form hexagonal pits so that the $[2\bar{1}\bar{1}0]$ direction could be identified based on the pit orientation. Graphene ribbons along $[2\bar{1}\bar{1}0]$ with widths of approximately 120 nm were then fabricated by electron-beam lithography and O_2-plasma etching at room temperature

© 2010 WILEY-VCH Verlag GmbH & Co. KGaA, Weinheim
WILEY InterScience DISCOVER SOMETHING GREAT

ADVANCED MATERIALS
www.advmat.de

Materials Views
www.MaterialsViews.com

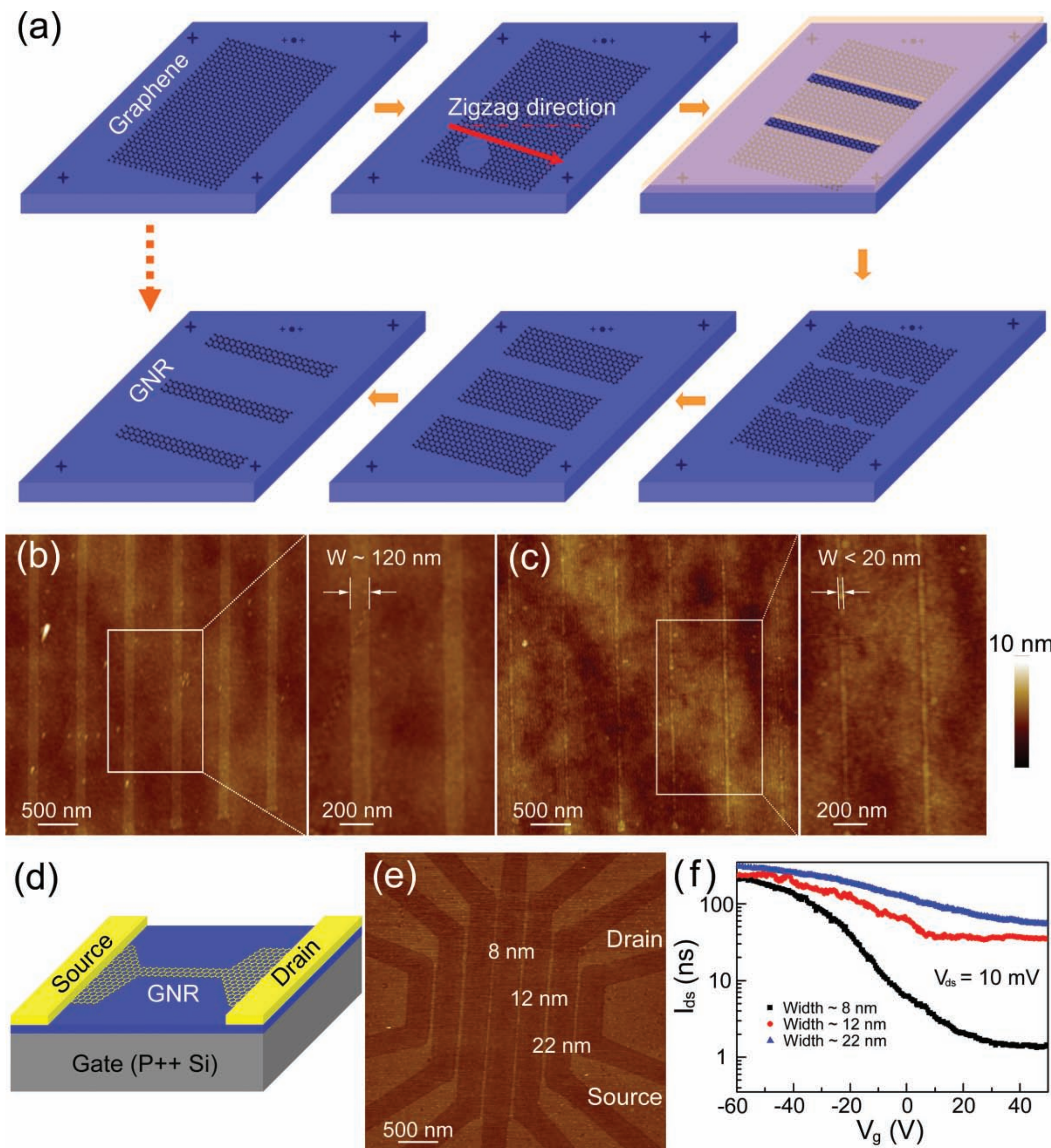

Figure 4. Fabrication of a GNR array along a designed crystallographic direction. a) Schematic procedures for fabricating a GNR array along a designated crystallographic direction using anisotropic etching. Graphene on SiO_2 with alignment marks was used as the starting material. It was first etched using a 50 W plasma for 10 min to form a few indicative hexagonal pits. Graphene crystallographic orientation was identified by imaging the hexagonal pits relative to the alignment marks. Graphene ribbon arrays along a designated crystallographic orientation were then fabricated by electron-beam lithography and O_2-plasma etching. Finally, GNR arrays were fabricated by reducing the ribbon width to sub-20 nm. b,c) AFM image for typical graphene patterns generated after O_2-plasma etching and after 50 W H_2-plasma etching at 500 °C for 6 min, respectively. The ribbon widths were measured by AFM under tip-radius correction. d) Schematic drawing of a GNR-FET using graphene as contact electrodes. e) AFM images of GNR-FETs with different ribbon widths. f) Room-temperature transfer characteristics of GNR-FETs at V_{ds}= 10 mV for three different widths: ≈22, ≈12, and ≈8 nm.

(Figure 4b). Finally, we reduced the 120 nm wide ribbons down to sub-20 nm by H_2-plasma etching (Figure 4c). GNRs with atomically smooth edges could be achieved by taking advantage of this anisotropic etching technique and post-etching high-temperature annealing.[27,28] Back-gated field-effect transistor (FET) devices were produced using the as-fabricated GNRs. In order to lower the contact resistance for the GNRs, we used graphene as contact electrodes that were wired for measurements using Ti/Au (2/20 nm) metal pads (Figure 4d). Figure 4e shows the AFM image of the GNR devices with different GNR widths. The ≈12 and ≈22 nm graphene nanoribbon FET (GNR-FET) devices show weak gate voltage modulation of

 WILEY InterScience DISCOVER SOMETHING GREAT © 2010 WILEY-VCH Verlag GmbH & Co. KGaA, Weinheim

the conductance with device on/off ratios usually less than 10 (Figure 4f). As a comparison, the ≈8 nm GNR behaves like a semiconductor with bandgaps due to quantum confinement. The on- and off- state current change upon gate-voltage modulation for this particular device is above 2 orders of magnitude. The resistance of this device is about 50 kΩ.

In conclusion, we have demonstrated a highly anisotropic, dry-etching method for graphite or graphene basal planes. The etching depends strongly on the crystallographic orientation, resulting in zigzag edge formation. The etching process is attributed to hydrogenation and volatilization of carbon atoms, with etching dynamics consistent with methane formation. This dry, anisotropic etching approach is ideally suited for graphene tailoring because the etching rates can be precisely controlled and the quality of the graphene can be preserved. This simple, clean, controllable, and scalable technique is also compatible with existing semiconductor processing technology. Assuming that a wafer-scale single-crystal graphene sample is available, this anisotropic etching technique would provide a useful tool for fabrication of large-scale graphene nanostructures when combined with standard lithographic techniques. Thus, a road can be paved for future integrated graphene nanodevices based on suitable starting materials and the method reported here.

Experimental Section

The anisotropic etching was performed in a home-made, remote plasma system. An inductively coupled plasma was generated at the entrance of a 4 in. quartz-tube furnace using a RF (13.56 MHz) coil. A three-zone furnace was used to heat the samples to the desired temperatures. The sample was placed at the centre of the furnace, separated from the RF coil region by a distance of ≈15 in. The plasma was generated outside the furnace and carried downstream to reach the sample. The pressure in the tube furnace was fixed at ≈0.35 Torr for all etching by flowing hydrogen at 30 sccm and vacuum pumping. The graphite used for etching is highly oriented pyrolytic grade (HOPG, grades ZYA from Structure Probe, Inc. (USA)). Graphene samples were prepared from both HOPG and Kish-graphite (purchased from Covalent Materials) using a mechanical cleavage method. Graphene peeled from Kish-graphite is usually in large sheets while graphene ribbons are easily located when peeled from HOPG. The room temperature STM imaging was carried out using a multimode nanoscope scanning probe microscopy (SPM) system (Veeco) in air with a Pt-Ir alloy tip. All atomic-resolution images in constant-height mode were taken at $V_s = 0.02$ V and $I = 2$ nA. The low-temperature STM measurement was performed in an ultrahigh-vacuum low-temperature STM (Omicron) with a base pressure of approximately 10^{-10} mbar. The experiments were performed at 77 K using electrochemically etched tungsten tips. The tip drift during the I–V measurement was less than 1 nm/h.

Raman spectroscopy was carried out using a Horiba Jobin Yvon LabRAM HR-800 Raman microscope ($\lambda = 532$ nm, power = 1 mW, beam spot: ≈1 μm). Graphene ribbons were deposited on 300 nm SiO_2, which was thermally grown on heavily p-doped Si. Multiple terminal backgated devices were fabricated by standard electron-beam lithography (Raith 150), metal deposition (electron-beam evaporation), and the lifting-off technique. All the electrical measurements were finished on an Agilent 4156C semiconductor analyzer at room temperature in air.

Supporting Information

Supporting Information is available online from Wiley InterScience or from the author.

Acknowledgements

This work was supported by the Institute of Physics (IOP) start-up funding, the 100 Talents Program of the Chinese Academy of Sciences (CAS), the Science Foundation of CAS (Grant no. 20091111100202), the National Science Foundation of China (NSFC) (Grant No. 10974226), and the National 973 Project of China (Grant No. 2010CB934202). We thank L. Lu, W. Liang, C. Gu, H. Zhou, L. Meng, and Q. Liu for technical assistance and discussions.

Received: February 18, 2010
Revised: April 12, 2010
Published online:

[1] A. K. Geim, K. S. Novoselov, *Nat. Mater.* **2007**, *6*, 183.
[2] A. K. Geim, *Science* **2009**, *324*, 1530.
[3] J. Chen, C. Jang, S. Xiao, M. Ishigami, M. S. Fuhrer, *Nat. Nanotechnol.* **2008**, *3*, 206.
[4] Y. Melinda, H. B. Özyilmaz, Y. Zhang, P. Kim, *Phys. Rev. Lett.* **2007**, *98*, 206805.
[5] C. Stampfer, J. Güttinger, S. Hellmüller, F. Molitor, K. Ensslin, T. Ihn, *Phys. Rev. Lett.* **2009**, *102*, 056403.
[6] V. Barone, O. Hod, G. E. Scuseria, *Nano Lett.* **2006**, *6*, 2748.
[7] Z. Chen, Y. Lin, M. J. Rooks, P. Avouris, *Physica E* **2007**, *40*, 228.
[8] K. A. Ritter, J. W. Lyding, *Nat. Mater.* **2009**, *8*, 235.
[9] L. A. Ponomarenko, F. Schedin, M. I. Katsnelson, R. Yang, E. W. Hill, K. S. Novoselov, A. K. Geim, *Science* **2008**, *320*, 356.
[10] K. Todd, H. T. Chou, S. Amasha, D. G. Gordon, *Nano Lett.* **2009**, *9*, 416.
[11] Y. W. Son, M. L. Cohen, S. G. Louie, *Nature* **2006**, *444*, 347.
[12] L. Yang, C. H. Park, Y. W. Son, M. L. Cohen, S. G. Louie, *Phys. Rev. Lett.* **2007**, *99*, 186801.
[13] P. G. Silvestrov, K. B. Efetov, *Phys. Rev. Lett.* **2007**, *98*, 016802.
[14] J. Fernandez-Rossier, J. J. Palacios, *Phys. Rev. Lett.* **2007**, *99*, 177204.
[15] S. Bhowmick, V. B. Shenoy, *J. Chem. Phys.* **2008**, *128*, 244717.
[16] A. K. Singh, B. I. Yakobson, *Nano Lett.* **2009**, *9*, 1540.
[17] J. Jung, A. H. MacDonald, *Phys. Rev. B* **2009**, *79*, 235433.
[18] M. Pumera, *Chem. Rec.* **2009**, *9*, 211.
[19] S. S. Datta, D. R. Strachan, S. M. Khamis, A. T. Charlie-Johnson, *Nano Lett.* **2008**, *8*, 1912.
[20] L. Ci, Z. Xu, L. Wang, W. Gao, F. Ding, K. F. Kelly, B. I. Yakobson, P. M. Ajayan, *Nano Res.* **2008**, *1*, 116.
[21] L. C. Campos, V. R. Manfrinato, J. D. Sanchez-Yamagishi, J. Kong, P. Jarillo-Herrero, *Nano Lett.* **2009**, *9*, 2600.
[22] F. Schäffel, J. H. Warner, A. Bachmatiuk, B. Rellinghaus, B. Büchner, L. Schultz, M. H. Rümmeli, *Nano Res.* **2009**, *2*, 695.
[23] P. Nemes-Incze, G. Magda, K. Kamarás, and L. P. Biró, *Nano Res.* **2010**, *3*, 110.
[24] B. J. Wood, H. Wise, *J. Phys. Chem.* **1969**, *73*, 1348.
[25] H. A. Mizes, J. S. Foster, *Science* **1989**, *244*, 559.
[26] P. Koskinen, S. Malola, H. Hakkinen, *Phys. Rev. Lett.* **2008**, *101*, 115502.
[27] X. T. Jia, M. Hofmann, V. Meunier, B. G. Sumpter, J. Campos-Delgado, J. M. Romo-Herrera, H. Son, Y. P. Hsieh, A. Reina, J. Kong, M. Terrones, M. S. Dresselhaus, *Science* **2009**, *323*, 1701.
[28] Ç. Girit, J. C. Meyer, R. Erni, M. D. Rossell, C. Kisielowski, L. Yang, C. Park, M. F. Crommie, M. L. Cohen, S. G. Louie, A. Zettl, *Science* **2009**, *323*, 1705.
[29] Z. Liu, K. Suenaga, P. J. F. Harris, S. Iijima, *Phys. Rev. Lett.* **2009**, *102*, 015501.
[30] Y. Niimi, T. Matsui, H. Kambara, K. Tagami, M. Tsukada, H. Fukuyama, *Phys. Rev. B* **2006**, *73*, 085421.

© 2010 WILEY-VCH Verlag GmbH & Co. KGaA, Weinheim

WILEY InterScience DISCOVER SOMETHING GREAT

[31] P. L. Giunta, S. P. Kelty, *J. Chem. Phys.* **2001**, *114*, 1807.
[32] T. Enoki, Y. Kobayashi, C. Katsuyama, V. Y. Osipov, M. V. Baidakova, K. Takai, K. Fukui, A. Y. Vul, *Diamond Related Mater.* **2007**, *16*, 2029.
[33] H. Xiang, E. Kan, S. Wei, M. Whangbo, J. Yang, *Nano Lett.* **2009**, *9*, 4025.
[34] Y. Kobayashi, K. Fukui, T. Enoki, K. Kusakabe, *Phys. Rev. B* **2006**, *73*, 125415.
[35] A. C. Ferrari, *Solid State Commun.* **2007**, *143*, 47.
[36] X. Li, X. Wang, L. Zhang, S. Lee, H. Dai, *Science* **2008**, *319*, 1229.
[37] X. Wang, Y. Ouyang, X. Li, H. Wang, J. Guo, H. Dai, *Phys. Rev. Lett.* **2008**, *100*, 206803.
[38] J. W. Bai, X. F. Duan, Y. Huang, *Nano Lett.* **2009**, *9*, 2083.
[39] L. Jiao, L. Zhang, X. Wang, G. Diankov, H. Dai, *Nature* **2009**, *458*, 877.
[40] D. V. Kosynkin, A. L. Higginbotham, A. Sinitskii, J. R. Lomeda, A. Dimiev, B. K. Price, J. M. Tour, *Nature* **2009**, *458*, 872.

© 2010 WILEY-VCH Verlag GmbH & Co. KGaA, Weinheim